A Classical Vacuum Spin Model for Propellantless Propulsion

Ioannis Xydous [1]

[1] BSc. E. Engineering, Piraeus, Greece, E-mail: ioannisxydous@gmail.com

A classical model of the vacuum as a continuum of massless spin carriers is developed and applied to propellantless propulsion. In this framework, a spacecraft imposes a standing electromagnetic wave with a position-dependent, time-varying phase gradient. The vacuum responds by generating a compensating spin current, and the reaction to this induced flow produces thrust without expelling propellant. The model reproduces reported asymmetric-capacitor forces and suggests that analogous effects may arise in magnetic configurations, to be examined in future work. It further indicates that a static phase gradient can reduce effective inertia by forming an inertial bubble that partially decouples the spacecraft interior from external acceleration. These mechanisms point to near-term applications in CubeSat-class probes for Earth-orbit and deep-space missions. The present work explores their implementation on such platforms while outlining a pathway from laboratory-scale devices to an inertial warp-drive concept—not by curving spacetime, but by reshaping inertia through controlled phase gradients or energy-density gradients.

DOI 10.5281/zenodo.20516763

I. INTRODUCTION

A number of reported experiments involving strong electrostatic field gradients or polarized materials—including the Exodus drive of Aurigema and Buhler [24], the Brown–Bahnson asymmetric capacitors [18, 19] as later tested by JLN Labs [14, 15], the T-shaped capacitor of Frolov [25], and the anomalous weight changes observed by Kita in polarized electrets [22]—suggest the possibility of thrust [11] or inertia modification [2, 3, 10, 12, 13, 23] without propellant. Although controversial, these results collectively point to a coupling between electromagnetic fields and vacuum structure not accounted for in standard electrodynamics. This work is motivated in part by Ivanov's Rhythmodynamics [21], which proposes that phase-shifted standing waves in the vacuum can generate force. Ivanov outlined the conceptual mechanism but did not provide a physical model describing how the vacuum interacts with a propelled object or the conditions required for sustained thrust. The present work addresses these gaps by introducing a classical model of the vacuum as a massless spin continuum obeying a spin-conservation law. In this framework, a spacecraft imposes a standing wave with a position-dependent, time-varying phase gradient. The vacuum responds by generating a compensating spin current, and the reaction to this induced flow produces thrust [1]. The same mechanism accounts for reported electrostatic thrust effects and suggests analogous behavior in magnetic configurations, which will be examined in future work. The model further implies that a static phase gradient can reduce effective inertia by forming an inertial bubble that partially decouples the spacecraft interior from external acceleration. Beyond these theoretical implications, the work explores near-term applications of the thrust mechanism to CubeSat-class probes for Earth-orbit station-keeping and deep-space missions. This provides a practical context for evaluating the propulsion architecture, while the broader inertial-bubble mechanism outlines a conceptual pathway toward an inertial warp-drive concept [16, 20], achieved not by curving spacetime [5, 17] but by reshaping inertia through controlled phase gradients. In this picture, net thrust arises from the integral of a moving phase gradient over the vacuum-coupled surface. A gradient propagating from low to high field strength produces a reaction opposite to its motion; reversing the propagation direction reverses the thrust. Opposing gradients cancel, so sustained unidirectional thrust requires a net moving phase pattern with a preferred direction. Momentum conservation remains intact because the vacuum, possessing intrinsic angular momentum, serves as the reaction partner. The ability to reshape inertia through controlled phase or energy-density gradients opens a conceptual pathway toward propulsion systems unconstrained by propellant mass. Such a capability would mark a profound technological shift, enabling efficient planetary transport, rapid interplanetary transfer, and eventually the possibility of interstellar exploration.

II. CLASSICAL VACUUM SPIN MODEL

We model the vacuum as a continuum of massless spin carriers (FIG. 1), where "classical spin" denotes an intrinsic angular-momentum property of each carrier. The local spin density $\rho_s(\vec{r},t)$ and its associated flow $\vec{J}_s(\vec{r},t)$ satisfy the continuity equation

$$\frac{\partial \rho_s}{\partial t} + \nabla \cdot \vec{J}_s = 0, \tag{1}$$

expressing that spin changes only through transport across a boundary and that the vacuum neither creates nor annihilates intrinsic angular momentum. In SI units, the spin density ρ_s has units of angular momentum per volume ($\mathrm{kg\,m^{-1}\,s^{-1}}$), while the spin current $\vec{J}_s$ has units of angular momentum per area per time ($\mathrm{kg\,s^{-2}}$). Both terms in Eq. (1) therefore share the same dimensions, confirming consistency.

A second conservation law, derived from Poynting's theorem, parallels the spin-continuity relation. Electromagnetic energy within any region changes only through energy flow across its boundary. The differential form is

$$\frac{\partial w_s}{\partial t} + \nabla \cdot \vec{S}_s = 0. \tag{2}$$

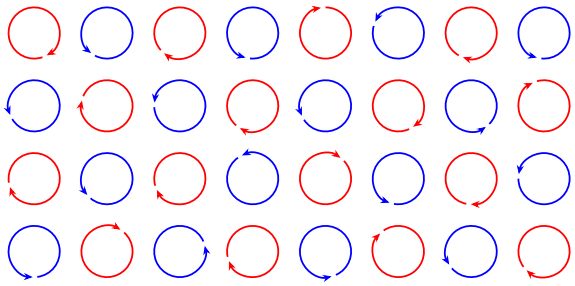

FIG. 1. **Classical vacuum illustration with massless spin.** The vacuum is modeled as a continuum of massless spin carriers (red and blue circles), with red and blue indicating opposite spin orientations in the unpolarized state. The field obeys the continuity relation $\partial_t \rho_s + \nabla \cdot \vec{J}_s = 0$, so spin can change only by flowing across boundaries. Under acceleration, matter attempts to reorient this distribution, and the vacuum resists through continuous realignment. This reaction manifests as inertia.

where w_s is the electromagnetic energy density and $\vec{S}_s$ is the Poynting vector.

In SI units, w_s has units of energy per volume (J m^{-3}), and $\vec{S}_s$ has units of energy per area per time (W m^{-2}). The term $\partial w_s/\partial t$ measures the rate of change of stored electromagnetic energy, while $\nabla \cdot \vec{S}_s$ gives the net outward energy flow. Their sum vanishing expresses local energy conservation.

III. SPACECRAFT THRUST EQUATION

A spacecraft is modeled as imposing an electromagnetic standing wave with phase $\phi(\vec{r}, t)$ that varies in both space and time. The resulting phase gradient drives an energy–carrying current in the surrounding vacuum,

$$\vec{J} = \kappa \, \nabla\phi, \tag{3}$$

where $\kappa > 0$ (units N/rad) is the vacuum response coefficient. This current represents the imposed motion of a phase or energy–density pattern across the spacecraft surface.

The vacuum responds to variations in the imposed energy-flow pattern, and the resulting reaction power density at the surface is

$$\vec{D}_{\text{thrust}} = -\frac{\partial \vec{J}}{\partial t} = -\kappa \, \frac{\partial}{\partial t} \nabla\phi. \tag{4}$$

Because $\vec{D}_{\text{thrust}}$ has the dimensions of a Poynting vector, we define

$$\vec{S}_{\text{vac}} \equiv \vec{D}_{\text{thrust}}, \tag{5}$$

interpreted as the vacuum–reaction Poynting vector associated with the driven motion of the phase or energy–density pattern.

The net force follows from integrating the reaction flux over the interacting surface and dividing by the pattern speed u_p:

$$\vec{F}_{\text{thrust}} = \frac{1}{u_p} \int_S \vec{S}_{\text{vac}} \, dS = -\frac{\kappa}{u_p} \, \frac{\partial}{\partial t} \int_S \nabla\phi \, dS. \tag{6}$$

Thrust requires both spatial and temporal variation of the phase,

$$\nabla\phi \neq 0, \qquad \frac{\partial \phi}{\partial t} \neq 0,$$

ensuring $\partial_t \nabla\phi \neq 0$. A stationary gradient produces no thrust. Reversing the propagation direction reverses the force. Multiple patterns superpose vectorially.

A full phase shift of π radians transfers maximum momentum. Dividing the energy density w over the surface area $A = \int_S dS$ by π yields the vacuum response coefficient

$$\kappa = \frac{wA}{\pi}. \tag{7}$$

Substituting into Eq. (6) gives

$$\vec{F}_{\text{thrust}} = -\frac{wA}{\pi u_p} \, \frac{\partial}{\partial t} \int_S \nabla\phi \, dS. \tag{8}$$

An equivalent formulation uses the spatial gradient of energy density:

$$\vec{F}_{\text{thrust}} = -\frac{A}{u_p} \, \frac{\partial}{\partial t} \int_S \nabla w \, dS, \tag{9}$$

linking thrust directly to a moving energy–density contrast.

In transient regimes the propagation speed of the charging front is not constant, so u_p cannot be treated as fixed. The thrust expression contains the local derivative $\partial/\partial t$, which governs the instantaneous buildup of the energy–density gradient $\nabla w(\vec{r}, t)$.

Introducing a finite transient duration Δt does not replace this derivative by a discrete difference. Instead, Δt enters only through the definition of the pattern speed, which characterizes the global propagation of the front.

An accelerating energy–density gradient necessarily implies a dynamical vacuum reaction. By Newton's third law, any force producing the acceleration of the gradient must be accompanied by a corresponding counter–force. In this model, the vacuum supplies that counterpart through an opposing Poynting flow. The accelerated gradient is therefore a physical entity rather than a mathematical artifact.

If the front starts from rest and traverses a path ΔL during the transient interval Δt, its displacement obeys $\Delta L = \frac{1}{2} a (\Delta t)^2$. This gives an average acceleration $a = 2\Delta L/(\Delta t)^2$. The corresponding average pattern speed is

$$\langle u_p \rangle = a \, \Delta t = \frac{2\Delta L}{\Delta t},$$

which replaces the constant–velocity assumption in the thrust expression. This finite–difference characterization of u_p enters only as a global parameter. The local time evolution of ∇w remains governed by the continuous derivative $\partial/\partial t$.

Consequently, the thrust relations

$$\vec{F}_{\text{thrust}} = \frac{1}{\langle u_p \rangle} \int_S \vec{S}_{\text{vac}} \, dS = -\frac{\kappa}{\langle u_p \rangle} \, \frac{\partial}{\partial t} \int_S \nabla\phi \, dS, \tag{10}$$

$$\vec{F}_{\text{thrust}} = -\frac{A}{\langle u_p \rangle} \, \frac{\partial}{\partial t} \int_S \nabla w \, dS. \tag{11}$$

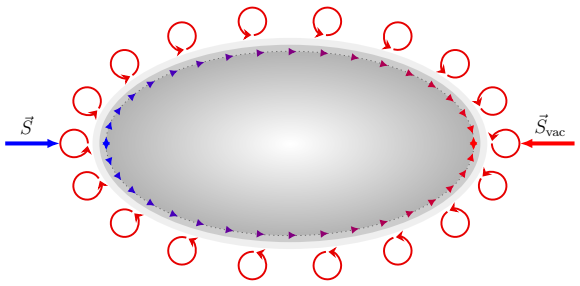

FIG. 2. **Spacecraft interaction with the vacuum.** A spatial phase gradient across the surface polarizes the surrounding vacuum, creating a stored energy–density contrast. When this gradient later varies in time, the phase or energy–density pattern sweeps across the surface, generating a Poynting vector $\vec{S}$. As the front advances, the vacuum releases the momentum accumulated during the earlier polarization, producing a reaction flow $\vec{S}_{\rm vac}$ opposite to the propagation direction.

remain valid in general. For a uniformly accelerated transient front one may insert $\langle u_p \rangle = 2\Delta L/\Delta t$ to obtain explicit scaling with the propagation path ΔL and transient duration Δt.

— *Why the thrust is not classical field reaction.* In standard electrodynamics, reaction forces arise only when electric charge undergoes free acceleration. The present mechanism differs fundamentally. Electrons remain confined within the metallic lattice and do not experience the large accelerations required for significant radiation reaction.

Thrust instead arises from the acceleration of an imposed energy–density gradient. This gradient interacts with the vacuum's internal angular–momentum polarization and produces a vacuum reaction force through momentum exchange with the structured vacuum background.

— *Geometric considerations.* A perfectly symmetric sphere cannot produce net thrust during transient charging because the surface integral of $\nabla w \cdot dS$ cancels over the closed boundary. Breaking the symmetry—by segmentation or material variation—allows a nonzero net flux.

An ellipsoid (FIG. 2) possesses a preferred axis. When the transient charging front propagates along the major axis, the projections of ∇w onto the outward normals no longer cancel, yielding directed thrust.

For open structures such as parallel–plate capacitors, momentum exchange occurs only through the open cross–section $A_{\rm cross} = W \cdot d$. The rest of the closed boundary contributes zero net flux. Thus, capacitors thrust through their open face, whereas closed bodies thrust through their entire closed boundary.

IV. ORIGIN OF INERTIA

The response coefficient κ quantifies the coupling between the spacecraft and the vacuum structure. In the thrust mechanism, this coupling governs how a moving energy–density pattern exchanges momentum with the vacuum.

The same coupling also determines the origin of inertia. In this model, resistance to acceleration arises not only from the intrinsic rest energy mc^2 but also from the interaction between matter and the vacuum's random angular–momentum polarization. In its natural isotropic state, this polarization opposes changes in motion, producing the familiar inertial reaction.

A static spatial structure—represented by a stationary gradient of electromagnetic energy density—partially aligns the vacuum polarization. Establishing this alignment requires work, since the initially random spin distribution must be reoriented. The required energy is drawn from the electromagnetic field, reducing the spacecraft's effective electromagnetic inertia.

The missing energy resides in the aligned vacuum configuration. Thus, the reduction reflects a change in the vacuum's opposition to acceleration rather than a change in rest mass.

This interpretation is reinforced by the dynamical behavior of the vacuum when an energy–density gradient is driven into acceleration. An accelerating gradient necessarily carries a Poynting vector and therefore a flux of field momentum.

By momentum conservation, such a flux cannot arise without a corresponding counter–momentum supplied by the vacuum. The vacuum must generate an opposing Poynting flow—its reaction force—to balance the momentum imparted to the accelerating pattern.

This is the field-theoretic expression of Newton's third law: forces in nature appear in pairs, and an accelerated energy configuration cannot exist without the vacuum providing its counterpart. Inertia therefore originates from the vacuum's response to changes in the motion of matter and of the imposed energy–density structure.

Let the vacuum have energy density w_0. With no imposed gradient, the energy in volume V is $U_0 = w_0 V$. Establishing a static energy–density gradient requires alignment energy $U_{\rm align}$, giving

$$U_{\rm total} = U_0 + U_{\rm align}. \tag{12}$$

For a closed spacecraft–vacuum system, total energy is conserved:

$$U_{\rm sc} + U_0 = \text{constant}, \tag{13}$$

so when the vacuum gains $U_{\rm align} > 0$, the spacecraft loses the same amount:

$$\Delta U_{\rm sc} = -U_{\rm align}. \tag{14}$$

If the spacecraft's effective inertia is proportional to the energy available to resist acceleration, the corresponding inertia change is

$$\Delta m = -\frac{U_{\rm align}}{u_0^2}, \tag{15}$$

where u_0 is the propagation speed of vacuum excitations (equal to c only if Lorentz symmetry holds).

For a static configuration, the alignment energy must depend on the structure of the energy–density gradient over the entire enclosing surface. The appropriate quantity is the surface integral

$$W_\nabla = \int_S |\nabla w|\, dS, \tag{16}$$

which measures the total imposed contrast of energy density across the spacecraft boundary.

The absolute value ensures that regions of opposite orientation contribute positively, since inertia reduction depends on the magnitude of alignment rather than its direction.

The alignment energy associated with a given surface-integrated gradient is

$$U_{\text{align}} = \zeta\, W_{\nabla}, \tag{17}$$

where ζ is a vacuum response coefficient.

Let $W_{\nabla,\max}$ denote the maximum attainable surface-integrated gradient. The corresponding maximum alignment energy is

$$U_{\text{align,max}} = \zeta\, W_{\nabla,\max}. \tag{18}$$

Assuming linear response, the effective inertia-reduction relation becomes

$$\frac{\Delta m}{m} = -\frac{U_{\text{align}}}{U_{\text{align,max}}} = -\frac{W_{\nabla}}{W_{\nabla,\max}}, \tag{19}$$

so the effective inertial mass is

$$m_i = m\left(1 - \frac{W_{\nabla}}{W_{\nabla,\max}}\right). \tag{20}$$

Uniform shielding requires ∇w to be constant over the enclosed surface. A uniformly charged sphere produces no gradient. A constant gradient on a closed surface requires a linearly varying field strength, which can be approximated using segmented electrodes.

The patent by R. Kita [22] describes an organic dielectric whose electron configuration changes under applied fields. In the present model, this corresponds to establishing a static gradient that reduces the material's effective inertia rather than altering gravitational coupling.

Once this gradient is imposed, the electromagnetic surface surrounding the spacecraft forms a coherent boundary layer—a vacuum-aligned shell that isolates the interior from external random polarization. All enclosed matter shares the same reduced inertia, so during acceleration the crew experiences no inertial forces.

With the bubble established, the process unfolds in two stages. First, a strong static gradient ∇w is generated to align the vacuum configuration and create the inertial bubble. Second, while this gradient is held constant, the reduced inertial mass m_i allows large accelerations from comparatively small external forces.

To decelerate or change direction, the gradient is weakened, removed, or reversed, restoring the normal inertial response.

Momentum conservation remains intact throughout. The "missing" momentum is stored in the aligned vacuum configuration itself. When the gradient is released, the vacuum relaxes back to its random state and returns this stored momentum as thrust, completing the exchange cycle.

The stored momentum and the resulting impulse is

$$\int \vec{F}_{\text{thrust}}\, dt = p_{\text{stored}} = (m - m_i)v = m\frac{W_{\nabla}}{W_{\nabla,\max}}v. \tag{21}$$

The shielding energy available is $U_{\text{align,max}}$. Comparing this to the spacecraft's equivalent energy $U_{\text{align,sc}}$ determines the degree of shielding:

$$U_{\text{align,max}} < U_{\text{align,sc}} \quad \text{partial shielding},$$

$$U_{\text{align,max}} = U_{\text{align,sc}} \quad \text{full shielding } (m_i = 0),$$

$$U_{\text{align,max}} > U_{\text{align,sc}} \quad \text{over-shielding}.$$

The ratio $U_{\text{align,max}}/U_{\text{align,sc}}$ bounds m_i between 0 and m. Negative inertia cannot occur because the available electromagnetic energy is finite.

This framework naturally explains why some experiments report transient effects but no steady-state inertia change. The experiments of Mikhailov [10, 12, 23], inspired by Assis [2, 3], attempted to measure mass reduction inside a charged spherical shell.

Assis, using Weber electrodynamics [4], obtained $m_i = m(1 - qV_E/3c^2)$. Mikhailov reported positive results, but independent replications found no steady-state effect.

Within the present model, this discrepancy is explained by transients. When the sphere is first charged, the charge distribution is non-uniform and evolves toward equilibrium. During this interval, the moving charge produces a time-varying energy-density gradient $\partial_t \nabla w \neq 0$, temporarily reducing inertia.

Once the distribution becomes uniform, the gradient vanishes and the effect disappears. Most replications measured only the steady state, explaining the null results. Sustained inertia reduction requires a non-uniform or segmented charge distribution to maintain a constant gradient across the surface.

V. FUNDAMENTAL VACUUM THRUSTER UNIT

The transient mechanism identified in the Mikhailov experiment applies directly to electrostatic propellantless thrusters whose operation depends on vacuum interaction rather than ion wind.

Relevant examples include the Exodus Drive [24], the Brown–Bahnson asymmetric capacitors [15, 19], Frolov's T-capacitors [14, 25], and the Poynting Flow Thruster (PFT) [6–9].

The PFT, introduced by Jean-Louis Naudin in 1999, demonstrates measurable thrust from a symmetric parallel-plate capacitor. Tests performed in sealed containers confirmed that the effect persists without airflow, ion wind, or convection, indicating that the reaction partner is the vacuum itself.

Because the vacuum permeates all space—including the interatomic and intra-atomic voids within matter—it cannot be shielded by massive objects. A vacuum-coupled thruster therefore remains fully operational even when enclosed within the hull of a spacecraft.

In the PFT, thrust appears only during charging and discharging transients, when a time-dependent spatial gradient of electromagnetic energy density exists. The dielectric increases the stored energy density, amplifying the effect.

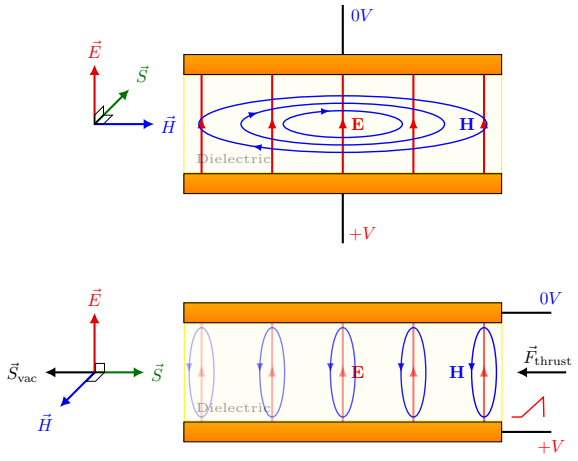

FIG. 3. **Fundamental vacuum thruster unit.** The top illustration shows a uniformly charging capacitor, where the inward Poynting flow is symmetric and no thrust is produced. In the transient case (bottom), the charging front spreads from the plate edges, creating a moving pattern of electric and magnetic fields throughout the dielectric volume. This evolving electromagnetic structure generates a Poynting vector $\vec{S}$ that propagates across the dielectric, forming a traveling energy-density gradient. The vacuum responds with an opposing reaction flow $\vec{S}_{\rm vac}$, producing a thrust force $\vec{F}_{\rm thrust}$ opposite to $\vec{S}$.

Within the present model, this behavior follows from Eqs. (10) and (11). A moving energy-density gradient interacts with the vacuum, and the reaction to this flow produces force.

— *PFT Parallel Plate Capacitor — Based on J. L. Naudin's Experiment* [7]. The device consists of two aluminum plates separated by a Plexiglas dielectric of thickness $d = 0.001$ m with relative permittivity $\varepsilon_r \approx 3.4$.

The plate length and width are $L = 0.12$ m and $W = 0.11$ m, respectively. High-voltage and ground leads are attached 10 mm from the plate edge.

The applied voltage is $V_0 = 30$ kV, giving a capacitance of approximately $C = 15$ pF and stored energy $U = 6.5$ mJ. The charging transient is estimated to have a rise time of $\Delta t_1 = 1$ s.

The total mass of the assembly is $m \approx 0.02$ kg, consisting of approximately 0.016 kg of Plexiglas for the dielectric and about 0.004 kg of aluminum for the 50 μm plates.

— *Electric field and energy density at the wire-fed edge*:

$$E = \frac{V_0}{d} = 3 \cdot 10^7 \text{ V/m}, \qquad w = \frac{1}{2}\varepsilon_0 \varepsilon_r E^2 \approx 1.35 \cdot 10^4 \text{ J/m}^3.$$

Plexiglas (PMMA) has a dielectric breakdown strength in the range of 15–60 MV/m, placing the applied field $E = 3 \cdot 10^7$ V/m near the upper limit of its transient withstand capability.

— *Energy density at the opposite edge*:

$$w_{\rm far} \approx 0.$$

— *Spatial gradient of energy density*:

$$|\nabla w| \approx \frac{w}{L} \approx \frac{1.35 \cdot 10^4}{0.12} \approx 1.125 \cdot 10^5 \text{ J/m}^4.$$

— *Interacting surface (open side face)*:

$$A_{\rm cross} = W \cdot d = 1.1 \cdot 10^{-4} \text{ m}^2.$$

— *Flux of ∇w through the open surface with efficiency η*:

$$\Phi \approx \eta \, |\nabla w| \, A_{\rm cross} \approx 6.18 \text{ J/m}^2, \qquad \eta = 0.5.$$

— *Time derivative of the flux*: The charging front travels the plate length L in time Δt_1, giving the transient-averaged pattern speed

$$\langle u_p \rangle = \frac{2L}{\Delta t_1} = 0.24 \text{ m/s}.$$

The corresponding flux rate is

$$\frac{\partial \Phi}{\partial t} \approx 6.18 \text{ W/m}^2.$$

— *Peak thrust*:

$$F_{\rm peak} = -\frac{A_{\rm cross}}{\langle u_p \rangle} \frac{\partial \Phi}{\partial t} \approx -2.8 \text{ mN}.$$

— *Charging phase* ($\Delta t_1 = 1$ s):

$$m \, \Delta v_1 = \frac{1}{2} F_{\rm peak} \Delta t_1 = -1.4 \cdot 10^{-3} \text{ N·s}, \qquad \Delta v_1 = -0.07 \text{ m/s}.$$

— *Discharging phase* ($\Delta t_2 = 1$ ms):

$$m \, \Delta v_2 = \frac{1}{2} F_{\rm peak} \Delta t_2 = 1.4 \cdot 10^{-6} \text{ N·s}, \qquad \Delta v_2 = 7.0 \cdot 10^{-5} \text{ m/s}.$$

— *Net impulse per cycle*:

$$\Delta p_{\rm net} = m\Delta v_1 + m\Delta v_2 \approx -1.4 \cdot 10^{-3} \text{ N·s}.$$

— *Average thrust*:

$$F_{\rm avg} = \frac{\Delta p_{\rm net}}{\Delta t_1 + \Delta t_2} \approx -1.4 \text{ mN}.$$

— *Thrust-to-power ratio*:

$$P_{\rm avg} = \frac{U}{\Delta t_1}, \qquad \frac{|F_{\rm avg}|}{|P_{\rm avg}|} \approx 0.21 \text{ N/W}.$$

A rapid discharge produces only a small reverse impulse, so the cycle yields a net unidirectional thrust.

The ultimate test for confirming a vacuum-reaction origin of the thrust is to repeat the experiment with the dielectric removed and the space between the plates evacuated of air, while keeping the plate spacing unchanged.

Under these conditions the electric field remains the same, but the energy density is reduced by the factor $\varepsilon_r \approx 3.4$. As a result, the average thrust decreases accordingly:

$$F_{\rm avg,v} = \frac{F_{\rm avg}}{\varepsilon_r} \approx -0.41 \text{ mN}.$$

The thrust-to-power ratio is reduced by the same factor:

$$\frac{|F_{\rm avg,v}|}{|P_{\rm avg,v}|} = \frac{1}{\varepsilon_r} \frac{|F_{\rm avg}|}{|P_{\rm avg}|} \approx 0.06 \text{ N/W}.$$

— *Mechanism*: In the PFT, both the high-voltage and return leads connect near the same plate edge (FIG. 3), producing asymmetric energy entry.

The top illustration shows the idealized case of symmetric feeding, where $\vec{S}$ is inward and no thrust occurs.

In the actual device, charging begins at the plate edges because the applied voltage launches an electromagnetic disturbance into the dielectric.

This disturbance propagates along the coaxial line as a moving voltage pattern, establishing a time-dependent electric and magnetic field configuration.

The propagating field carries a Poynting vector $\vec{S}$ that sweeps through the dielectric volume, forming a traveling energy-density gradient.

The free electrons in the conductors do not propagate with the signal; they merely shift locally to satisfy boundary conditions.

The vacuum responds to the motion of the field gradient with an opposing reaction flow $\vec{S}_{\text{vac}}$, producing a thrust force $\vec{F}_{\text{thrust}}$ opposite to $\vec{S}$.

The bottom illustration of FIG. 3 depicts this state just before the charge becomes uniform.

Once the voltage stabilizes and the plates reach uniform charge, the gradient vanishes and thrust drops to zero.

Each new voltage increase initiates another transient. During discharge, the gradient reverses and a counter-thrust is produced.

To obtain net forward thrust, this reverse impulse must be minimized. A sawtooth waveform (FIG. 3) naturally provides the required asymmetry: the slow voltage rise produces a long forward impulse, while the rapid discharge yields only a brief counter-thrust, resulting in net unidirectional force.

VI. COAXIAL LINE VACUUM THRUSTER

The capacitor thruster (FIG. 3) demonstrates that a directed Poynting vector within a dielectric is the essential ingredient for generating a reaction force from the vacuum.

A coaxial transmission line (FIG. 4) naturally satisfies this requirement. Its geometry constrains the electromagnetic energy flow to be strictly axial and confined to the dielectric between the conductors.

Although coaxial cables are typically used for high-frequency signals, long-duration asymmetric voltage pulses can drive a similarly directed Poynting flux. In this regime the line acts as a guided conduit for a unidirectional energy-density gradient, enabling it to operate as a vacuum-reaction thruster.

— *Coaxial Line Experimental Proposal*. The coaxial-line configuration (FIG. 4) considered here is based on a standard RG-58/U transmission line. Its geometry confines the electromagnetic fields to the ring-shaped dielectric region between the conductors and forces the Poynting vector to remain strictly axial.

This directly parallels the parallel-plate thruster: in both cases the mechanism relies on establishing a directed Poynting vector through a dielectric region, and the coaxial structure enforces this condition by design.

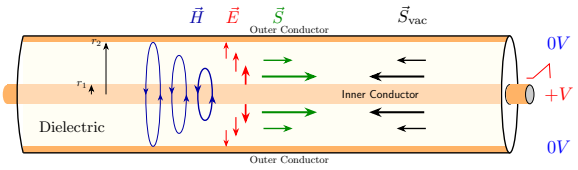

FIG. 4. **Coaxial Line Vacuum Thruster.** The coaxial-line vacuum thruster confines the fields to the ring-shaped dielectric region between the conductors, where the electric field $\vec{E}$ is radial, the magnetic field $\vec{H}$ is azimuthal, and their cross product forms an axial Poynting vector $\vec{S}$. A long asymmetric pulse drives a traveling front of $\vec{E}$ and $\vec{H}$ along the line, producing a directed energy flow through the dielectric. In this model the vacuum responds with an opposing reaction flow $\vec{S}_{\text{vac}}$, generating a transient thrust opposite to $\vec{S}$.

The cable consists of a solid polyethylene dielectric with relative permittivity $\varepsilon_r \approx 2.25$. It surrounds a central copper conductor of diameter $d_{\text{in}} = 0.90\,\text{mm}$ and is enclosed by an outer conductor with inner diameter $D_{\text{out}} = 3.00\,\text{mm}$.

The dielectric has an outer diameter of $D_{\text{diel}} = 2.95\,\text{mm}$, defining a field region spanning the radii $r_1 = 0.45\,\text{mm}$ to $r_2 = 1.475\,\text{mm}$ along a coaxial section of length $L = 0.12\,\text{m}$.

Within this volume the electric field $\vec{E}$ is radial, the magnetic field $\vec{H}$ is azimuthal, and the resulting Poynting vector $\vec{S} = \vec{E}\times\vec{H}$ is purely axial and fully confined to the dielectric.

Although the polyethylene dielectric in RG-58/U has a theoretical breakdown strength of 20–40 MV/m, the cable is not designed to withstand such stress for extended durations. Its specified maximum working voltage is about 300 V, with a short-term test rating of 1.5–2.5 kV.

These limits are set by practical concerns such as heating, partial discharge, and long-term insulation reliability. A 1 s pulse approaches a quasi-DC condition, so only a small fraction of the material's theoretical dielectric strength can be safely used.

In practice, pulse amplitudes of a few kilovolts are realistic for a 1 s excitation. Operation near the 20–40 kV material limit would entail a substantial risk of breakdown.

As in the parallel-plate thruster, only the transient regime contributes to thrust. The guided-wave geometry of the coaxial line ensures that the Poynting vector remains parallel to the cable axis, so a long-duration asymmetric pulse establishes a unidirectional energy-density gradient whose reaction with the vacuum produces an axial force.

— *Electric field and energy density in the coaxial dielectric*: For the RG-58/U geometry with inner and outer radii r_1 and r_2 and an applied voltage $V_0 = 10\,\text{kV}$, the radial electric field is

$$E(r) = \frac{V_0}{r\ln(r_2/r_1)}.$$

At the inner conductor surface this gives

$$E_{\max} = \frac{V_0}{r_1\ln(r_2/r_1)} \approx 1.87\cdot 10^7\ \text{V/m},$$

which remains below the transient dielectric strength of polyethylene (20–40 MV/m).

The corresponding peak energy density is

$$w_{\max} = \tfrac{1}{2}\varepsilon_0\varepsilon_r E_{\max}^2 \approx 3.49 \cdot 10^3\ \mathrm{J/m^3}.$$

A more representative value is obtained from the cross-sectional average of E^2 over the dielectric region:

$$\langle E^2 \rangle = \frac{\displaystyle\int_{r_1}^{r_2} E^2(r)\, 2\pi r\, dr}{\displaystyle\int_{r_1}^{r_2} 2\pi r\, dr} = \frac{2V_0^2}{(r_2^2 - r_1^2)\,\ln(r_2/r_1)}.$$

Inserting this into the energy-density expression yields

$$\langle w \rangle = \frac{1}{2}\,\varepsilon_0\varepsilon_r\,\langle E^2 \rangle \approx 8.5 \cdot 10^2\ \mathrm{J/m^3}.$$

— *Spatial gradient of energy density along the line*: Over the active coaxial length $L = 0.12$ m, the energy density decreases from $\langle w \rangle$ near the pulse front to approximately zero behind it. This gives an average axial gradient

$$|\nabla w| \approx \frac{\langle w \rangle}{L} \approx \frac{8.5 \cdot 10^2}{0.12} \approx 7.1 \cdot 10^3\ \mathrm{J/m^4}.$$

— *Interacting cross-section*: The relevant cross-sectional area of the dielectric is

$$A_{\mathrm{cross}} = \pi(r_2^2 - r_1^2) \approx 6.2 \cdot 10^{-6}\ \mathrm{m^2}.$$

— *Flux of* ∇w *through the cross-section with efficiency* η:

$$\Phi \approx \eta\,|\nabla w|\,A_{\mathrm{cross}}, \qquad \eta = 0.5,$$

so that

$$\Phi \approx 0.5 \cdot 7.1 \cdot 10^3 \cdot 6.2 \cdot 10^{-6} \approx 2.2 \cdot 10^{-2}\ \mathrm{J/m^2}.$$

— *Time derivative of the flux*: For a charging time $\Delta t_1 = 1$ s, the transient-averaged pattern speed is

$$\langle u_p \rangle = \frac{2L}{\Delta t_1} = 0.24\ \mathrm{m/s}.$$

The corresponding flux rate is

$$\frac{\partial \Phi}{\partial t} \approx \frac{\Phi}{\Delta t_1} \approx 2.2 \cdot 10^{-2}\ \mathrm{W/m^2}.$$

— *Peak thrust*:

$$F_{\mathrm{peak}} = -\frac{A_{\mathrm{cross}}}{\langle u_p \rangle}\frac{\partial \Phi}{\partial t} \approx -\frac{6.2 \cdot 10^{-6}}{0.24} \cdot 2.2 \cdot 10^{-2} \approx -5.7 \cdot 10^{-7}\ \mathrm{N}.$$

— *Charging phase* ($\Delta t_1 = 1$ s):

$$m\,\Delta v_1 = \frac{1}{2} F_{\mathrm{peak}} \Delta t_1 \approx -2.9 \cdot 10^{-7}\ \mathrm{N{\cdot}s}.$$

— *Discharging phase* ($\Delta t_2 = 1$ ms):

$$m\,\Delta v_2 = \frac{1}{2} F_{\mathrm{peak}} \Delta t_2 \approx 2.9 \cdot 10^{-10}\ \mathrm{N{\cdot}s}.$$

— *Net impulse per cycle*:

$$\Delta p_{\mathrm{net}} = m\Delta v_1 + m\Delta v_2 \approx -2.9 \cdot 10^{-7}\ \mathrm{N{\cdot}s}.$$

— *Average thrust*:

$$F_{\mathrm{avg}} = \frac{\Delta p_{\mathrm{net}}}{\Delta t_1 + \Delta t_2} \approx -2.9 \cdot 10^{-7}\ \mathrm{N}.$$

— *Stored energy and thrust-to-power ratio*: The capacitance per unit length of the coaxial line is

$$C' = \frac{2\pi\varepsilon_0\varepsilon_r}{\ln(r_2/r_1)}.$$

For a length L the total capacitance is $C = C'L \approx 12.6$ pF, giving a stored energy

$$U = \frac{1}{2}CV_0^2 = \frac{\pi\varepsilon_0\varepsilon_r L}{\ln(r_2/r_1)}\,V_0^2 \approx 6.3 \cdot 10^{-4}\ \mathrm{J}.$$

With a charging time $\Delta t_1 = 1$ s, the average input power is

$$P_{\mathrm{avg}} = \frac{U}{\Delta t_1} \approx 6.3 \cdot 10^{-4}\ \mathrm{W}.$$

The corresponding thrust-to-power ratio is

$$\frac{|F_{\mathrm{avg}}|}{|P_{\mathrm{avg}}|} \approx \frac{2.9 \cdot 10^{-7}}{6.3 \cdot 10^{-4}} \approx 4.6 \cdot 10^{-4}\ \mathrm{N/W}.$$

The much smaller thrust obtained for the coaxial line compared with the capacitor thruster follows directly from the geometry and field distribution.

In the coaxial case the effective interacting cross-section is only the narrow annular region between the conductors, several orders of magnitude smaller than the open side face of the parallel-plate configuration.

At the same time the axial energy-density gradient is greatly reduced, since the stored energy per unit length of the coaxial line is limited by its small capacitance and the modest field levels that can be applied without risking dielectric breakdown.

The product $A_{\mathrm{cross}} \cdot |\nabla w|$ is therefore far lower than in the capacitor thruster, leading naturally to a correspondingly weaker vacuum-reaction force.

Additionally, the coaxial-line experiment serves a second purpose. It demonstrates that, with appropriate dielectric materials and enlarged cross-sectional geometries, future coaxial structures could be engineered to achieve significantly higher thrust levels using standard manufacturing techniques.

VII. THIN FILM CAPACITOR FABRICATION WITH BARIUM TITANATE

Thin-film capacitors utilizing Barium Titanate ($BaTiO_3$) as the dielectric material are fully manufacturable using standard power-electronics fabrication processes.

The fabrication sequence begins with the deposition of a bottom metal electrode onto a substrate. This is followed by deposition of the $BaTiO_3$ thin film using techniques such as chemical solution deposition (sol-gel), sputtering, or pulsed-laser deposition.

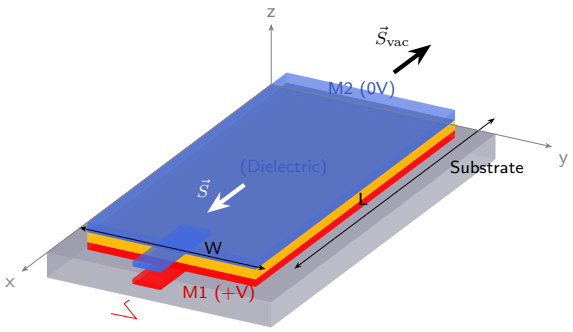

FIG. 5. **Thin Film Capacitor Vacuum Thruster.** A $BaTiO_3$ (yellow) thin-film capacitor driven by an asymmetric charging pulse. During the charging interval, the electromagnetic energy flow $\vec{S}$ propagates across the dielectric thickness, forming a directed energy-density gradient along the film. This moving pattern induces a vacuum reaction flow $\vec{S}_{vac}$ that opposes $\vec{S}$, producing a net thrust on the structure. Because the interacting surface is the thin dielectric edge, the resulting force is concentrated along the narrow cross-section of the film, yet remains fully analogous in mechanism to the parallel-plate capacitor thruster.

A high-temperature annealing step crystallizes the film into the perovskite phase, imparting its high dielectric constant and ferroelectric properties. Finally, a top metal electrode is deposited to complete the Metal–Insulator–Metal (MIM) capacitor structure.

These processes are well-established in semiconductor manufacturing, demonstrating that such capacitor designs are practically achievable with existing fabrication infrastructure.

A representative thin-film capacitor for propulsion experiments can be realized as a MIM structure (FIG. 5) using sintered bulk $BaTiO_3$ as the dielectric.

We consider a rectangular active area of length $L = 0.01\,\mathrm{m}$ and width $W = 0.01\,\mathrm{m}$, with a $BaTiO_3$ layer of thickness $d = 1\,\mathrm{mm}$ and relative permittivity $\varepsilon_r \approx 2560$.

The corresponding capacitance is

$$C = \varepsilon_0 \varepsilon_r \frac{L \cdot W}{d} \approx 2.27 \cdot 10^{-9}\,\mathrm{F}.$$

The breakdown field of 1.8 kV/mm allows an operating voltage up to $V_{max} \approx 1.8\,\mathrm{kV}$ across the dielectric.

The electrodes can be implemented as copper films of thickness $d_{Cu} \approx 10\,\mu\mathrm{m}$ on a ceramic substrate (e.g. alumina) of thickness $d_{sub} \approx 0.5\,\mathrm{mm}$.

The active area is

$$A = L \cdot W = 1.0 \cdot 10^{-4}\,\mathrm{m}^2.$$

The dielectric volume is

$$V_{BaTiO_3} = A \cdot d = 1.0 \cdot 10^{-7}\,\mathrm{m}^3,$$

and with density $\rho_{BaTiO_3} \approx 6.02 \cdot 10^3\,\mathrm{kg/m}^3$ the dielectric mass is

$$m_{BaTiO_3} \approx 6.02 \cdot 10^{-4}\,\mathrm{kg} \quad (0.602\,\mathrm{g}).$$

The two copper electrodes have a combined volume

$$V_{Cu} = 2A \cdot d_{Cu} = 2.0 \cdot 10^{-9}\,\mathrm{m}^3,$$

so for $\rho_{Cu} \approx 8.96 \cdot 10^3\,\mathrm{kg/m}^3$,

$$m_{Cu} \approx 1.79 \cdot 10^{-5}\,\mathrm{kg} \quad (0.0179\,\mathrm{g}).$$

The substrate volume is

$$V_{sub} = A \cdot d_{sub} = 0.5 \cdot 10^{-7}\,\mathrm{m}^3,$$

and with $\rho_{sub} \approx 3.9 \cdot 10^3\,\mathrm{kg/m}^3$ (alumina),

$$m_{sub} \approx 1.95 \cdot 10^{-4}\,\mathrm{kg} \quad (0.195\,\mathrm{g}).$$

The total mass of the component (dielectric, electrodes, substrate) is therefore

$$m_{tot} \approx m_{BaTiO_3} + m_{Cu} + m_{sub} \approx 0.81 \cdot 10^{-3}\,\mathrm{kg} \quad (0.81\,\mathrm{g}).$$

— *Electric field and energy density in the $BaTiO_3$ dielectric*: For the $BaTiO_3$ slab with thickness $d = 1\,\mathrm{mm}$ and applied voltage $V_0 = 1000\,\mathrm{V}$, the electric field is

$$E = \frac{V_0}{d} = \frac{1000}{10^{-3}} = 1.0 \cdot 10^6\,\mathrm{V/m}.$$

The corresponding energy density is

$$w = \frac{1}{2}\varepsilon_0 \varepsilon_r E^2 \approx 1.13 \cdot 10^4\,\mathrm{J/m}^3.$$

— *Energy density at the opposite edge*:

$$w_{far} \approx 0.$$

— *Spatial gradient of energy density along the plate*: For a plate length $L = 0.01\,\mathrm{m}$, the average axial energy-density gradient is

$$|\nabla w| \approx \frac{w}{L} \approx \frac{1.13 \cdot 10^4}{0.01} \approx 1.13 \cdot 10^6\,\mathrm{J/m}^4.$$

— *Interacting surface (open side face)*:

$$A_{cross} = W \cdot d = 0.01 \cdot 10^{-3} = 1.0 \cdot 10^{-5}\,\mathrm{m}^2.$$

— *Flux of ∇w through the open surface with efficiency η*:

$$\Phi \approx \eta\,|\nabla w|\,A_{cross}, \qquad \eta = 0.5,$$

so that

$$\Phi \approx 0.5 \cdot 1.13 \cdot 10^6 \cdot 1.0 \cdot 10^{-5} \approx 5.65\,\mathrm{J/m}^2.$$

— *Time derivative of the flux*: For a charging time $\Delta t_1 = 1\,\mathrm{s}$, the transient-averaged pattern speed is

$$\langle u_p \rangle = \frac{2L}{\Delta t_1} = \frac{2 \cdot 0.01}{1} = 0.02\,\mathrm{m/s}.$$

The corresponding flux rate is

$$\frac{\partial \Phi}{\partial t} \approx \frac{\Phi}{\Delta t_1} \approx 5.65\,\mathrm{W/m}^2.$$

— *Peak thrust*:

$$F_{\text{peak}} = -\frac{A_{\text{cross}}}{\langle u_p \rangle}\frac{\partial \Phi}{\partial t} \approx -\frac{1.0 \cdot 10^{-5} \cdot 5.65}{0.02} \approx -2.82 \cdot 10^{-3}\,\text{N}.$$

— *Charging phase* ($\Delta t_1 = 1$ s):

$$m\,\Delta v_1 = \frac{1}{2} F_{\text{peak}} \Delta t_1 \approx -1.41 \cdot 10^{-3}\,\text{N·s}.$$

— *Discharging phase* ($\Delta t_2 = 10$ ms):

$$m\,\Delta v_2 = \frac{1}{2} F_{\text{peak}} \Delta t_2 \approx 1.41 \cdot 10^{-5}\,\text{N·s}.$$

— *Net impulse per cycle*:

$$\Delta p_{\text{net}} = m\Delta v_1 + m\Delta v_2 \approx -1.41 \cdot 10^{-3}\,\text{N·s}.$$

— *Average thrust*:

$$F_{\text{avg}} = \frac{\Delta p_{\text{net}}}{\Delta t_1 + \Delta t_2} \approx -1.41 \cdot 10^{-3}\,\text{N}.$$

— *Stored energy and thrust-to-power ratio*: The capacitance of the $BaTiO_3$ slab is

$$C = \varepsilon_0 \varepsilon_r \frac{L \cdot W}{d} \approx 2.27 \cdot 10^{-9}\,\text{F},$$

so that the stored energy at $V_0 = 1000$ V is

$$U = \frac{1}{2} C V_0^2 \approx 1.13 \cdot 10^{-3}\,\text{J}.$$

With $\Delta t_1 = 1$ s,

$$P_{\text{avg}} = \frac{U}{\Delta t_1} \approx 1.13 \cdot 10^{-3}\,\text{W},$$

and the corresponding thrust-to-power ratio is

$$\frac{|F_{\text{avg}}|}{|P_{\text{avg}}|} \approx \frac{1.41 \cdot 10^{-3}}{1.13 \cdot 10^{-3}} \approx 1.24\,\text{N/W}.$$

VIII. CUBESAT-CLASS FEASIBILITY STUDY FOR VACUUM-THRUSTER PROPULSION

— *Current CubeSat propulsion technologies*. Current small-spacecraft propulsion technologies span a broad range of thrust levels and efficiencies.

Cold-gas thrusters typically provide 0.1–0.15 N for basic attitude and orbit control. *Warm-gas and resistojet systems* offer 0.1–0.2 N with modestly improved performance. *Chemical micropropulsion* delivers 0.1–1 N and supports rapid, high-Δv maneuvers.

At lower force levels, *electric propulsion*—ion and RF thrusters—operates in the 1–10 mN range with very high specific impulse suitable for long-duration missions.

Non-propellant systems such as photon-pressure or sail-based concepts generate micronewton forces but can operate continuously without expending mass.

Hybrid *electrolysis-based microthrusters* reach peak thrusts of 0.5–1 N and are increasingly used in CubeSat platforms.

Together, these systems define the operational envelope against which alternative propulsion concepts, including vacuum–coupling thrusters, must be evaluated.

— *CubeSat-class mass and volume*. The feasibility of applying vacuum–thruster propulsion to a CubeSat-class space probe is examined using a compact one-unit form-factor platform equipped with a dedicated vacuum–coupling propulsion module.

A representative mass allocation begins with a conventional 2.8 kg one-unit platform integrating the structural chassis, avionics suite, mission payload, battery pack, and the charging–discharging circuitry required to support the propulsion system.

In standard CubeSat practice, the structure constitutes the largest portion of this mass. Avionics, payload, and the battery follow, with the battery providing roughly 150 Wh of usable energy.

Before evaluating thrust, the mass of a fully manufactured thin-film capacitor unit must be established. Each unit has an intrinsic component mass of 0.81 g, with an additional 0.39 g allocated for spacing, routing, and structural closing.

Thus, the mass per complete thin-film capacitor unit is

$$m_{\text{unit}} \approx 0.81\,\text{g} + 0.39\,\text{g} \approx 1.20\,\text{g}.$$

To the baseline platform, the vacuum–thruster module is added as a self-contained subsystem comprising 1000 thruster units on each external face, for a total of 6000 units.

The propulsion-module mass is

$$m_{\text{units}} = 6000\, m_{\text{unit}} \approx 7.2\,\text{kg},$$

and the total space-probe mass becomes

$$m_{\text{probe}} = 2.8\,\text{kg} + 7.2\,\text{kg} \approx 10\,\text{kg}.$$

This configuration enables both attitude and altitude control. Attitude control governs rotational behavior such as antenna pointing, solar-panel orientation, instrument alignment, and stabilization.

Altitude control addresses translational maneuvers including orbit maintenance, station-keeping, and deorbit operations.

For attitude control, thruster units on each face are arranged into two diagonal sub-groups. Pure rotation is achieved by activating diagonally opposite sub-groups on two opposing faces simultaneously. Translational components cancel while torques add.

The power subsystem can reverse the polarity of the thrust-capacitor banks on any face, enabling either acceleration or deceleration. When two opposite faces are activated in parallel, the probe can generate a two-fold increase in net acceleration along the corresponding axis.

Nevertheless, all thrust and mission-profile calculations in this and the following sections consider activation of a single face only, providing a conservative baseline.

— *Volume analysis*. A fully manufactured thin-film capacitor unit has total mass

$$m_{\text{unit}} = 0.81\,\text{g} + 0.39\,\text{g} \approx 1.20\,\text{g}.$$

The geometric volumes of the three main components are

$$V_{\mathrm{BaTiO_3}} = 1.0 \cdot 10^{-7}\,\mathrm{m}^3, \quad V_{\mathrm{Cu}} = 2.0 \cdot 10^{-9}\,\mathrm{m}^3, \quad V_{\mathrm{sub}} = 5.0 \cdot 10^{-8}\,\mathrm{m}^3,$$

giving a total assembly volume

$$V_{\mathrm{tot}} = V_{\mathrm{BaTiO_3}} + V_{\mathrm{Cu}} + V_{\mathrm{sub}} \approx 1.52 \cdot 10^{-7}\,\mathrm{m}^3.$$

Assuming the additional 0.39 g has similar average density, the volume of one fully manufactured unit scales as

$$V_{\mathrm{unit}} \approx V_{\mathrm{tot}} \frac{m_{\mathrm{unit}}}{m_{\mathrm{tot}}} \approx 2.25 \cdot 10^{-7}\,\mathrm{m}^3.$$

For 6000 units, the aggregate capacitor-unit volume is

$$V_{\mathrm{units}} = 6000\, V_{\mathrm{unit}} \approx 1.35 \cdot 10^{-3}\,\mathrm{m}^3.$$

A standard 1U CubeSat face has area

$$A_{\mathrm{face}} \approx 0.10 \cdot 0.10 = 1.0 \times 10^{-2}\,\mathrm{m}^2.$$

Dividing the total thruster volume across six faces gives

$$V_{\mathrm{face}} = \frac{V_{\mathrm{units}}}{6} \approx 2.25 \times 10^{-4}\,\mathrm{m}^3.$$

The corresponding thruster-layer thickness on each face is

$$d_{\mathrm{thruster}} = \frac{V_{\mathrm{face}}}{A_{\mathrm{face}}} \approx 2.25 \times 10^{-2}\,\mathrm{m}.$$

Thus, a fully populated 6000-unit propulsion module forms an outer shell of thickness ~ 2.3 cm on each face, increasing the external envelope from the nominal 0.10 m CubeSat size to approximately 0.145 m in the relevant dimension. The spacecraft remains CubeSat-derived but operates outside conventional deployer constraints.

Vacuum-thruster units may operate either directly exposed to space or from within the chassis, since vacuum permeates all materials and cannot be shielded.

— *Thrust per face*. Using the thin-film capacitor thrust unit value $F_{\mathrm{avg}} \approx -1.41 \cdot 10^{-3}$ N, the average thrust per face is

$$F_{\mathrm{avg,face}} = |1000 \cdot F_{\mathrm{avg}}| \approx 1.41\,\mathrm{N}.$$

— *Power per face*. The average electrical power required per face is

$$P_{\mathrm{avg,face}} = 1000 \cdot P_{\mathrm{avg}} \approx 1.13\,\mathrm{W}.$$

A continuous 1 h thrust interval processes

$$U_{\mathrm{thrust,face}} = 3600 \cdot P_{\mathrm{avg,face}} \approx 4.07 \times 10^3\,\mathrm{J} \quad (1.13\,\mathrm{Wh}),$$

which is only 0.75% of a 150 Wh battery.

To avoid repeatedly drawing this processed energy from the battery, the electrical subsystem employs a *bidirectional, high-efficiency DC–DC converter* that returns capacitor energy to the low-voltage bus after each discharge.

Assuming converter efficiency $\eta_{\mathrm{conv}} \approx 0.95$ and 5% ohmic loss, the total loss fraction is $\sim 10\%$. Thus, the actual battery expenditure per hour is

$$U_{\mathrm{loss}} \approx 0.10\, U_{\mathrm{thrust,face}} \approx 0.113\,\mathrm{Wh}.$$

Consequently, the thrust-capacitor system operates in a loss-limited regime. Nearly all reactive energy circulates through the charge–discharge cycles and is recovered, while the battery supplies only conversion losses.

With a loss of 0.113 Wh per hour, a 150 Wh battery can sustain continuous thrust for

$$t_{\mathrm{battery}} = \frac{150\,\mathrm{Wh}}{0.113\,\mathrm{Wh/h}} \approx 1327\,\mathrm{h} \quad (\approx 55\,\mathrm{days}).$$

Solar panels can easily supply the required 0.113 W average loss, enabling uninterrupted thrust capability under illumination.

— *Acceleration per face*. The acceleration delivered by a single face is

$$a_{\mathrm{probe}} = \frac{F_{\mathrm{avg,face}}}{m_{\mathrm{probe}}} \approx 0.141\,\mathrm{m/s}^2.$$

After 1 h of continuous thrust,

$$u_{\mathrm{probe}} = a_{\mathrm{probe}} \cdot 3600 \approx 507.6\,\mathrm{m/s}.$$

The distance covered in the same interval is

$$d_{\mathrm{travel}} = \frac{1}{2} a_{\mathrm{probe}} \cdot \Delta t^2 \approx 9.136 \cdot 10^5\,\mathrm{m} \quad (913.6\,\mathrm{km}).$$

— *Controlled discharge and high-efficiency energy return path*. Thrust is produced only during the charging interval of the high-voltage capacitor C_{T}. Once the target potential of ~ 1000 V is reached, thrust stops and the capacitor must be discharged.

Charging occurs over ~ 1 s, while discharging must complete within 1–100 ms. Direct dumping would waste energy and is unsuitable.

Each active face is connected through a *bidirectional DC–DC converter* linking the 1000 V thruster node to the low-voltage bus. Forward mode slowly charges C_{T}; reverse mode rapidly extracts stored energy and returns it to the bus.

Inductor-based or resonant topologies enable controlled, low-loss millisecond-scale recovery.

This bidirectional path allows each thrust cycle to be powered primarily by recovered energy, with the battery supplying only conversion losses and net vacuum-coupled energy.

A CubeSat-derived probe equipped with such vacuum thrusters can maintain orbit indefinitely, provided sufficient electrical power is available. Operational lifetime is limited not by orbital mechanics but by non-orbital factors such as solar-array degradation, electronics failures, battery aging, or loss of attitude-control capability.

IX. CUBESAT-CLASS PROBE FOR DEEP-SPACE MISSIONS

In this section we develop approximate thrust and energy requirements for a CubeSat-derived probe capable of traveling from Earth (ISS) to Mars, continuing to Pluto, and returning to the ISS.

For mission planning we adopt the maximum heliocentric separations between Earth and the target bodies. This ensures a conservative estimate of travel distance and energy demand.

The Earth–Mars separation can reach up to 400 million km when the planets lie on opposite sides of the Sun. The Earth–Pluto separation can extend to approximately 7.5 billion km near Pluto's aphelion.

These upper-bound distances provide a robust basis for evaluating thrust, transit time, and power requirements of the proposed propulsion architecture.

— *100-hour thrust interval*. Applying the findings from the previous section, a CubeSat-derived probe equipped with a 150 Wh energy-storage system can operate the vacuum-thrust mechanism on a single face for a total activation time of

$$\Delta t = 3.6 \cdot 10^5 \text{ s} \quad (100 \text{ h}).$$

Using the previously derived face-acceleration a_{probe}, the resulting cruise velocity after this thrust interval is

$$u = a_{\text{probe}} \cdot \Delta t \approx 5.076 \cdot 10^4 \text{ m/s}.$$

The distance covered during continuous thrusting over the same interval is

$$d_{100\text{h}} = \tfrac{1}{2} a_{\text{probe}} (\Delta t)^2 \approx 9.13 \cdot 10^9 \text{ m}.$$

The required energy processed by the propulsion system during this interval is

$$U_{\text{thrust, face}} = P_{\text{avg, face}} \cdot \Delta t \approx 406.8 \text{ kJ} \quad (113 \text{ Wh}).$$

This processed energy corresponds to roughly 75% of the available 150 Wh battery capacity. However, the bidirectional DC–DC converter recovers nearly all capacitor energy from each thrust interval, so the battery supplies only irreversible losses.

— *Battery expenditure*. With converter efficiency $\eta_{\text{conv}} \approx 0.95$ and an additional 5% ohmic loss, the total effective loss fraction is $\sim 10\%$.

Thus, for a processed energy of $U_{\text{processed}} \approx 113$ Wh, the corresponding battery drain becomes

$$U_{\text{loss}} \approx 0.10 \cdot 113 \text{ Wh} \approx 11.3 \text{ Wh}.$$

For the round trip, the thrust sequence (acceleration, braking, return-acceleration, braking) therefore requires

$$U_{\text{loss, 4 phases}} \approx 4 \cdot 11.3 \text{ Wh} \approx 45.2 \text{ Wh},$$

leaving more than 100 Wh of the 150 Wh battery capacity available for other spacecraft functions.

A standard 150 Wh CubeSat battery can sustain continuous thrust for

$$t_{\text{battery}} = \frac{150 \text{ Wh}}{0.113 \text{ Wh/h}} \approx 1327 \text{ h} \quad (\approx 55 \text{ days}),$$

before exhausting its usable charge.

Since the vacuum-thruster system requires only 0.113 Wh per hour, the battery capacity is more than sufficient for any single 100 h thrust interval and for four such intervals per mission.

Solar panels oriented toward the Sun during thrusting can continuously replenish the battery. Under typical CubeSat power budgets, the solar array easily supplies the required 0.113 W average loss.

The probe retains the attitude- and translation-control capabilities described previously, allowing both precise torque generation and pure linear acceleration depending on the selected activation pattern.

— *Earth to Mars and back*. For an Earth–Mars separation of $4 \cdot 10^{11}$ m, the remaining distance after acquiring the cruise speed u is

$$d_{\text{(E-M), rem}} = 4 \cdot 10^{11} - d_{100\text{h}} \approx 3.91 \cdot 10^{11} \text{ m}.$$

The time required to cover this remaining distance is

$$t_{\text{(E–M), rem}} = \frac{d_{\text{(E–M), rem}}}{u} \approx 7.7 \cdot 10^6 \text{ s} \quad (89.1 \text{ days}).$$

For a symmetric outbound and return leg, the total Earth–Mars round-trip time becomes

$$t_{\text{(E–M), tot}} \approx 2\, t_{\text{(E–M), rem}} \approx 1.54 \cdot 10^7 \text{ s} \quad (178.2 \text{ days}).$$

To bring the probe to rest outside Mars' sphere of influence ($R_{\text{SOI,Mars}} \approx 5.8 \cdot 10^8$ m), the vacuum thruster must be operated in deceleration mode for an additional 100 h.

A corresponding 100 h thrust phase is required for the return acceleration, and a final 100 h deceleration phase near Earth completes the symmetric profile.

The total processed propulsion energy for these four thrust phases is

$$U_{\text{thrust, (E–M), tot}} \approx 4 \cdot U_{\text{thrust,face}} \approx 1.63 \text{ MJ} \quad (452 \text{ Wh}),$$

internally circulated within the capacitor–converter system.

The corresponding battery expenditure is

$$U_{\text{loss, (E–M), tot}} \approx 4 \cdot U_{\text{loss}} \approx 45.2 \text{ Wh},$$

which remains well within the 150 Wh capacity.

— *Earth to Pluto and back*. For an Earth–Pluto separation of $7.5 \cdot 10^{12}$ m, the remaining distance after acquiring the cruise speed u is

$$d_{\text{(E-P), rem}} = 7.5 \cdot 10^{12} - d_{100\text{h}} \approx 7.4909 \cdot 10^{12} \text{ m}.$$

The time required to traverse this remaining distance is

$$t_{\text{(E-P), rem}} = \frac{d_{\text{(E-P), rem}}}{u} \approx 1.4757 \cdot 10^8 \text{ s} \quad (1708 \text{ days}).$$

To bring the probe to rest outside Pluto's sphere of influence ($R_{\mathrm{SOI,Pluto}} \approx 3.0 \cdot 10^9$ m), the vacuum thruster must again be operated in deceleration mode for 100 h.

A symmetric 100 h thrust phase is required for the return acceleration, followed by a final 100 h deceleration phase near Earth.

The energy requirements for the Earth–Pluto round trip mirror the Earth–Mars case:

$$U_{\mathrm{thrust,\,(E–P),\,tot}} \approx 4 \cdot U_{\mathrm{thrust,\,face}} \approx 1.63\,\mathrm{MJ} \quad (452\,\mathrm{Wh}),$$

internally circulated within the capacitor–converter system.

The associated battery expenditure is

$$U_{\mathrm{loss,\,(E–P),\,tot}} \approx 4 \cdot U_{\mathrm{loss}} \approx 45.2\,\mathrm{Wh}.$$

The corresponding Earth–Pluto round-trip travel time is

$$t_{\mathrm{(E–P),\,tot}} \approx 2\,t_{\mathrm{(E–P),\,rem}} \approx 3.416 \cdot 10^3\,\mathrm{days} \quad (3416\,\mathrm{days}),$$

demonstrating that a 150 Wh CubeSat battery can support four full 100 h thrust phases for deep-space missions while retaining substantial energy margin.

X. NEXT-GENERATION CUBESAT-CLASS PROBE FOR DEEP-SPACE MISSIONS

Calcium copper titanate ($CaCu_3Ti_4O_{12}$, CCTO) is a perovskite-related oxide ceramic distinguished by its colossal bulk permittivity, typically $\varepsilon_r \sim 10^4 - 10^5$ at room temperature when processed as sintered pellets.

In the present architecture, this property is utilized by fabricating CCTO as macroscopic dielectric blocks of 10 mm×10 mm× 1 mm. These blocks are produced through conventional ceramic processing—powder compaction followed by high-temperature sintering—to preserve the internal-barrier-layer microstructure responsible for the high permittivity.

Each block is metallized on its opposing faces to form an individual parallel-plate capacitor. Multiple units are combined to obtain the required total capacitance.

Although these elements operate as bulk ceramic capacitors rather than microfabricated films, their footprint and stacking geometry remain compatible with a compact electronics module. This provides a practical route to very high capacitance densities within the available volume of the thrust-capacitor assembly.

This grouped CCTO approach also aligns with established automated manufacturing methods used in high-power capacitor modules. For each CubeSat face, 1000 CCTO blocks are assembled into electrically parallel banks, providing the required bulk capacitance for thrust generation.

The activation pattern of these banks preserves the same attitude- and translation-control capabilities described previously, enabling both torque generation and pure linear acceleration without specialized geometric subdivision.

Interconnection is achieved through common copper bus layers bonding all top and bottom electrodes. This mirrors the shared-metallization strategy of thin-film capacitor arrays but implemented at the millimeter scale using automated pick-and-place assembly and robotic alignment.

Applied consistently across all CubeSat-Class Probe faces, this configuration provides high-capacitance thrust banks suitable for orbit control and deep-space acceleration while relying entirely on mature, scalable manufacturing processes standard in power-electronics production.

Assuming a CCTO formulation can be engineered to achieve a dielectric constant nearly one hundred times that of sintered barium titanate, i.e. $\varepsilon_r \approx 2.65 \times 10^5$, such a material would enable an unprecedented increase in capacitance density within the proposed thrust-capacitor architecture.

It is also worth noting that the adoption of CCTO does not introduce a mass penalty relative to conventional $BaTiO_3$ dielectrics. Sintered barium titanate has a bulk density of approximately 6.0 g/cm^3, whereas $CaCu_3Ti_4O_{12}$ typically exhibits a lower density of about 4.7 g/cm^3. This $\sim 21\%$ reduction in dielectric mass is significant and can be utilized either to accommodate additional thruster units or to allocate more mass to the payload.

In parallel, the power subsystem is assumed to employ a next-generation 6000 Wh battery with the same mass as current 150 Wh CubeSat-class units. This corresponds to a roughly forty-fold increase in specific energy (Wh/kg).

Such future battery capacity is required to support four consecutive long-duration thrust phases: 100 h acceleration, 100 h braking, 100 h reverse acceleration for the return leg, and 100 h braking before Earth.

The combination of a lighter high-permittivity dielectric and a high-density battery preserves the overall mass budget while enabling substantially longer thrust durations and enhanced mission capability.

— Thrust per face (enhanced CCTO dielectric). With the original barium titanate thin-film units, the average thrust per face for 1000 capacitors was

$$F_{\mathrm{avg,face}}^{(\mathrm{BaTiO_3})} = |1000 \cdot F_{\mathrm{avg}}| \approx 1.41\,\mathrm{N}.$$

Assuming a CCTO formulation with a dielectric constant increased by a factor of 100, the thrust per unit scales accordingly. The average thrust per face for the same 1000 units becomes

$$F_{\mathrm{avg,face}}^{(\mathrm{CCTO})} \approx 141\,\mathrm{N}.$$

— Processed power and battery usage (CCTO, 6000 Wh storage). The processed reactive power per face scales in the same proportion, increasing from

$$P_{\mathrm{avg,face}}^{(\mathrm{BaTiO_3})} \approx 1.13\,\mathrm{W} \quad \text{to} \quad P_{\mathrm{avg,face}}^{(\mathrm{CCTO})} \approx 113\,\mathrm{W}.$$

A continuous 1 h thrust interval processes

$$U_{\mathrm{thrust,face}}^{(\mathrm{CCTO})} = 3600 \cdot P_{\mathrm{avg,face}}^{(\mathrm{CCTO})} \approx 4.07 \cdot 10^5\,\mathrm{J} \quad (113\,\mathrm{Wh}).$$

With a bidirectional, high-efficiency DC–DC converter recovering the capacitor energy after each discharge, the battery supplies only conversion losses. Using a converter efficiency of $\eta_{\mathrm{conv}} \approx 0.95$ and including an additional 5% ohmic loss, the total loss fraction becomes approximately 10%.

The battery drain per hour is therefore

$$U_{\mathrm{loss}}^{(\mathrm{CCTO})} \approx 0.10 \cdot 113\,\mathrm{Wh} \approx 11.3\,\mathrm{Wh}.$$

A 6000 Wh battery can thus sustain

$$t_{\max} \approx \frac{6000\,\mathrm{Wh}}{11.3\,\mathrm{Wh/h}} \approx 531\,\mathrm{h}$$

of continuous thrust, exceeding the required 400 h mission profile.

The required average processed power of 113 W is compatible with modern bidirectional DC–DC converters operating in a pulsed-thrust regime. Each cycle consists of a $\sim$ 1 s charging ramp followed by a fast discharge in the 1–100 ms range.

— Acceleration, velocity, and distance (CCTO, 1 h and 100 h). For the same probe mass m_{probe}, the acceleration per face increases from

$$a_{\mathrm{probe}}^{(\mathrm{BaTiO_3})} \approx 0.141\,\mathrm{m/s^2}$$

to

$$a_{\mathrm{probe}}^{(\mathrm{CCTO})} = \frac{F_{\mathrm{avg,face}}^{(\mathrm{CCTO})}}{m_{\mathrm{probe}}} \approx 14.1\,\mathrm{m/s^2}.$$

The escape velocity from Earth's gravitational field at the surface is

$$u_{\mathrm{esc}} = \sqrt{\frac{2GM_\oplus}{R_\oplus}} \approx 1.118 \cdot 10^4\,\mathrm{m/s}.$$

If the CubeSat-Class probe were hypothetically launched from Earth's surface using only the CCTO vacuum-thruster, the net upward acceleration would be

$$a_{\mathrm{net}} = a_{\mathrm{probe}}^{(\mathrm{CCTO})} - g \approx 4.29\,\mathrm{m/s^2}.$$

The time required to reach escape velocity would be

$$t_{\mathrm{esc}} = \frac{u_{\mathrm{esc}}}{a_{\mathrm{net}}} \approx 2.61 \cdot 10^3\,\mathrm{s} \quad (\approx 43.5\,\mathrm{min}).$$

The corresponding distance from Earth's surface would be

$$d_{\mathrm{esc}} = \tfrac{1}{2} a_{\mathrm{net}} t_{\mathrm{esc}}^2 \approx 1.46 \cdot 10^7\,\mathrm{m} \approx 2.3 R_\oplus.$$

In practice, though feasible in principle, this surface-launch scenario is not realistic. Atmospheric drag in the dense lower atmosphere would overwhelm the available thrust, and the vacuum-thruster is intended for near-vacuum operation rather than use within a thick atmospheric column.

For deep-space missions, the probe is assumed to be deployed from a carrier vehicle already outside the dense atmosphere and near orbital or escape conditions.

After 1 h of continuous thrust:

$$u_{\mathrm{probe}}^{(\mathrm{CCTO,1h})} \approx 5.08 \cdot 10^4\,\mathrm{m/s},$$

and the corresponding travel distance is

$$d_{\mathrm{travel}}^{(\mathrm{CCTO,1h})} \approx 9.14 \cdot 10^7\,\mathrm{m}.$$

Extending to 100 h of constant acceleration (idealized):

$$u_{\mathrm{probe}}^{(\mathrm{CCTO,100h})} \approx 5.08 \cdot 10^6\,\mathrm{m/s},$$

and the resulting covered distance is

$$d_{\mathrm{travel}}^{(\mathrm{CCTO,100h})} \approx 9.14 \cdot 10^{11}\,\mathrm{m}.$$

— From Earth to Mars and back. Using the 100 h thrust parameters:

$$u_{\mathrm{probe}}^{(\mathrm{CCTO,100h})} \approx 5.08{\cdot}10^6\,\mathrm{m/s}, \qquad d_{\mathrm{travel}}^{(\mathrm{CCTO,100h})} \approx 9.14{\cdot}10^{11}\,\mathrm{m}.$$

For an Earth–Mars separation of

$$d_{(\mathrm{E–M})} = 4.0 \cdot 10^{11}\,\mathrm{m},$$

the travel time from constant-acceleration motion is

$$t_{(\mathrm{E–M})} = \sqrt{\frac{2d_{(\mathrm{E–M})}}{a_{\mathrm{probe}}^{(\mathrm{CCTO})}}} \approx 2.38 \cdot 10^5\,\mathrm{s} \quad (\approx 66.1\,\mathrm{h}).$$

Since this is shorter than the 100 h thrust window, the probe reaches Mars during acceleration. Controlled arrival requires half-acceleration and half-deceleration:

$$t_{\mathrm{acc}} \approx 33.05\,\mathrm{h}, \qquad t_{\mathrm{dec}} \approx 33.05\,\mathrm{h}.$$

The total outbound time is

$$t_{(\mathrm{E–M),\,out}} \approx 66.1\,\mathrm{h}.$$

For a symmetric return leg:

$$t_{(\mathrm{E–M),\,tot}}^{(\mathrm{CCTO})} \approx 132.2\,\mathrm{h} \quad (\approx 5.5\,\mathrm{days}).$$

Processed propulsion energy per phase:

$$U_{\mathrm{thrust,phase}}^{(\mathrm{CCTO})} \approx 3.73 \cdot 10^3\,\mathrm{Wh},$$

so for four phases:

$$U_{\mathrm{thrust,\,(E–M),\,tot}} \approx 1.49 \cdot 10^4\,\mathrm{Wh}.$$

Battery expenditure:

$$U_{\mathrm{loss,\,(E–M),\,tot}} \approx 1.49 \cdot 10^3\,\mathrm{Wh},$$

well within the 6000 Wh capacity.

— From Earth to Pluto and back. For an Earth–Pluto separation of

$$d_{(\mathrm{E–P})} = 7.5 \cdot 10^{12}\,\mathrm{m},$$

the remaining distance after 100 h acceleration is

$$d_{(\mathrm{E–P),\,rem}}^{(\mathrm{CCTO})} \approx 6.59 \cdot 10^{12}\,\mathrm{m}.$$

Cruise time:

$$t_{(\mathrm{E–P),\,rem}}^{(\mathrm{CCTO})} \approx 1.30 \cdot 10^6\,\mathrm{s} \quad (\approx 15.0\,\mathrm{days}).$$

One-way time:

$$t_{(\mathrm{E–P),\,one}}^{(\mathrm{CCTO})} \approx 1.66 \cdot 10^6\,\mathrm{s}.$$

Round-trip time:

$$t^{(\mathrm{CCTO})}_{(\mathrm{E–P}),\,\mathrm{tot}} \approx 3.32 \cdot 10^6\,\mathrm{s} \quad (\approx 38.4\,\mathrm{days}).$$

Processed propulsion energy:

$$U_{\mathrm{thrust,(E–P),tot}} = 400\mathrm{h} \cdot 113\,\mathrm{Wh/h} = 45200\,\mathrm{Wh},$$

battery expenditure:

$$U_{\mathrm{loss,(E–P),tot}} = 0.1 \cdot U_{\mathrm{thrust,(E–P),tot}} \approx 4520\,\mathrm{Wh},$$

within the 6000 Wh capacity.

— *From Earth to Voyager 1 and back.* Voyager 1 is approximately one light-day from Earth:

$$d_{\mathrm{V1}} \approx 2.592 \cdot 10^{13}\,\mathrm{m}.$$

Its cruise speed is

$$u_{\mathrm{V1}} \approx 1.70 \cdot 10^4\,\mathrm{m/s}.$$

After 100 h thrust:

$$u^{(\mathrm{CCTO,100h})}_{\mathrm{probe}} \approx 5.08 \cdot 10^6\,\mathrm{m/s},$$

remaining distance:

$$d_{\mathrm{V1,\,rem}} \approx 2.5006 \cdot 10^{13}\,\mathrm{m}.$$

Relative velocity:

$$u_{\mathrm{rel}} \approx 5.063 \cdot 10^6\,\mathrm{m/s}.$$

Coast time:

$$t_{\mathrm{V1,\,rem}} \approx 4.94 \cdot 10^6\,\mathrm{s} \quad (\approx 57.2\,\mathrm{days}).$$

One-way time:

$$t^{(\mathrm{CCTO})}_{\mathrm{V1,\,one}} = 100\,\mathrm{h} + t_{\mathrm{V1,\,rem}} \approx 5.3 \cdot 10^6\,\mathrm{s}.$$

Round-trip time:

$$t^{(\mathrm{CCTO})}_{\mathrm{V1,\,tot}} \approx 1.05 \cdot 10^7\,\mathrm{s} \quad (\approx 122\,\mathrm{days}).$$

Battery expenditure:

$$U_{\mathrm{loss,\,V1,\,tot}} = 4520\,\mathrm{Wh},$$

within the 6000 Wh capacity.

— *From Earth to Proxima Centauri b.* Proxima Centauri b is approximately

$$d_{\mathrm{PCb}} \approx 4.018 \cdot 10^{16}\,\mathrm{m}.$$

After 100 h thrust:

$$u^{(\mathrm{CCTO,100h})}_{\mathrm{probe}} \approx 5.08 \cdot 10^6\,\mathrm{m/s},$$

remaining distance:

$$d_{\mathrm{PCb,\,rem}} \approx 4.018 \cdot 10^{16}\,\mathrm{m}.$$

Cruise time:

$$t_{\mathrm{PCb,\,rem}} \approx 7.91 \cdot 10^9\,\mathrm{s} \approx 250.7\,\mathrm{years}.$$

One-way time:

$$t^{(\mathrm{CCTO})}_{\mathrm{PCb,\,one}} \approx 250.7\,\mathrm{years}.$$

Thus, even with enhanced CCTO dielectric and a 100 h high-acceleration thrust phase, the CubeSat-Class probe would still require approximately 251 years to reach Proxima Centauri b.

This analysis excludes any form of inertial shielding that could arise when a CubeSat-class probe is embedded within a controllable static energy-density gradient. Such a configuration could, in principle, enable superluminal effective transit velocities if paired with future high-density batteries or alternative power-generation sources.

The results reported here therefore pertain exclusively to the thrust requirements and performance characteristics of the proposed vacuum-reaction thruster architecture, independent of any additional inertial-modification mechanisms.

XI. INERTIAL WARP DRIVE

The concept of a warp drive is most widely associated with the Alcubierre metric, a general-relativistic solution in which spacetime is engineered to contract in front of a spacecraft and expand behind it.

Propulsion is achieved not by accelerating the craft through space, but by deforming the spacetime geometry around it. Although consistent with Einstein's field equations, such configurations require exotic stress–energy distributions and remain far beyond known physical capabilities.

In contrast to general-relativistic warp drives that deform spacetime, an inertial warp drive modifies the spacecraft's inertial response by engineering its interaction with the vacuum.

Rather than bending the metric, the mechanism reshapes the effective inertia within a controlled region surrounding the craft.

This effect is produced (FIG. 2) by imposing a spatial phase gradient across the surface. Once established, the surrounding vacuum becomes polarized.

When the gradient then varies in time, the phase or energy-density pattern propagates across the surface, generating a Poynting vector $\vec{S}$ associated with the moving pattern.

As this advancing gradient releases the momentum stored during the earlier polarization, the vacuum responds with a counter-flow $\vec{S}_{\mathrm{vac}}$ directed opposite to the propagation.

A natural question arises: would such a mechanism violate Einstein's framework of special relativity, particularly its connection between velocity and increasing inertia?

Before deriving the mathematical extension of the theory, it is useful to recall the physical picture.

In the section on the origin of inertia, we saw that inertia—the resistance of matter to acceleration—emerges from the vacuum's reaction to changes in motion.

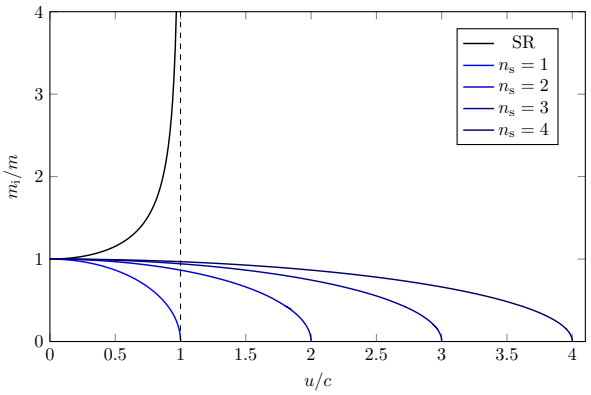

FIG. 6. **Relativistic inertia.** In special relativity (SR), the inertial mass m_i increases with speed u, diverging as u approaches the speed of light c. In contrast, when inertia reduction is applied in synchrony with increasing velocity, the effective inertia m_i can decrease with u, reaching zero and permitting velocities u that may exceed the speed of light c.

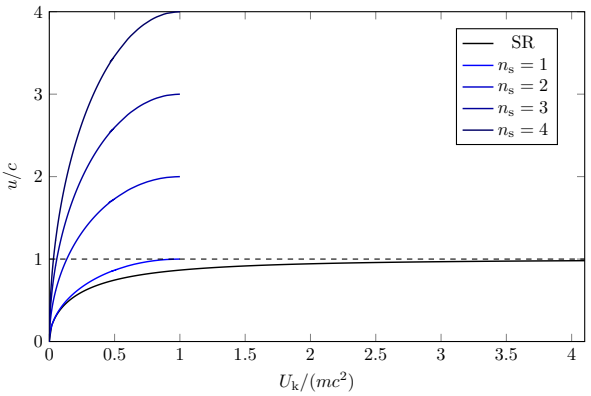

FIG. 7. **Relativistic velocity.** In SR, the kinetic energy may increase without bound, yet the velocity never exceeds c. With synchronized inertia reduction, the effective light-speed barrier becomes $n_s c$, allowing velocities beyond c when $n_s > 1$.

A spatial energy-density gradient reduces the vacuum's reactive response, lowering the effective inertia of the spacecraft.

Without such polarization, the inertia of a body increases with speed, as dictated by Einstein's formulation.

But with a controllable reduction of inertia, the situation reverses: the effective inertia can *decrease* as speed increases.

If the resistance to acceleration diminishes rather than grows, the usual relativistic barrier loses its foundation.

This leads to an important question: if inertia can be engineered downward as velocity rises, does the notion of a fundamental speed limit still hold?

Based on the previously derived inertia expression (Eq. (20)), we now clarify how the inertial mass m appears in

$$m_i = m\left(1 - \frac{W_\nabla}{W_{\nabla,\max}}\right) = m\left(1 - \frac{U_{\text{align}}}{U_{\text{align,max}}}\right). \tag{22}$$

When inertia is coupled to the vacuum, the expression indicates that it is tied to a specific energy scale $U_{\text{align,max}}$.

This implies an association with the interaction surface enclosing the spacecraft.

There must therefore exist a baseline energy that scales with the effective interaction area—an energy scale that, together with u_0, must ultimately be determined either experimentally or theoretically.

Furthermore, $U_{\text{align,max}}$ represents the maximum attainable alignment permitted by the spacecraft's available stored energy.

This value may be larger or smaller than the shielding energy $U_{\text{align,sc}}$ required for the spacecraft.

We consider an ellipsoidal spacecraft, as illustrated in FIG. 2. Its structure may consist of a single functional layer, in which propulsion and inertial shielding operate in parallel, or of two distinct layers: an outer shell dedicated to propulsion and an inner shell used exclusively for inertial shielding.

Starting with the Minkowski line element,

$$ds^2 = -c^2dt^2 + dx^2 + dy^2 + dz^2, \tag{23}$$

and assuming motion only along the x–direction, this reduces to

$$ds^2 = -c^2dt^2 + dx^2. \tag{24}$$

To incorporate the inertia-reduction effect into the metric, we scale the line element by $(m_i/m)^2$ and introduce an additional scaling n_s^2 to represent the maximum available stored energy.

This yields

$$ds^2 = -n_s^2c^2d\tau^2\left(\frac{m_i}{m}\right)^2. \tag{25}$$

Applying the same scaling to the coordinate form of the metric gives

$$ds^2 = -n_s^2c^2dt^2 + n_s^2dx^2. \tag{26}$$

Using the kinematic relation $n_s\,dx = u\,dt$, we obtain

$$ds^2 = -n_s^2c^2dt^2 + u^2dt^2. \tag{27}$$

Relating this to the proper time expression,

$$-n_s^2c^2d\tau^2\left(\frac{m_i}{m}\right)^2 = \left[-n_s^2c^2 + u^2\right]dt^2, \tag{28}$$

Dividing by $-n_s^2c^2$ yields

$$d\tau^2\left(\frac{m_i}{m}\right)^2 = \left[1 - \frac{u^2}{n_s^2c^2}\right]dt^2, \tag{29}$$

from which we obtain

$$\frac{dt}{d\tau} = \left(\frac{m_i}{m}\right)\frac{1}{\sqrt{1 - \frac{u^2}{n_s^2c^2}}}. \tag{30}$$

The relation between the stored energy $U_{\text{align,max}}$ and the scaling factor n_s is given by

$$\frac{U_{\text{align}}}{U_{\text{align,max}}} = \frac{U_{\text{align}}}{n_s^2U_{\text{align,sc}}}, \tag{31}$$

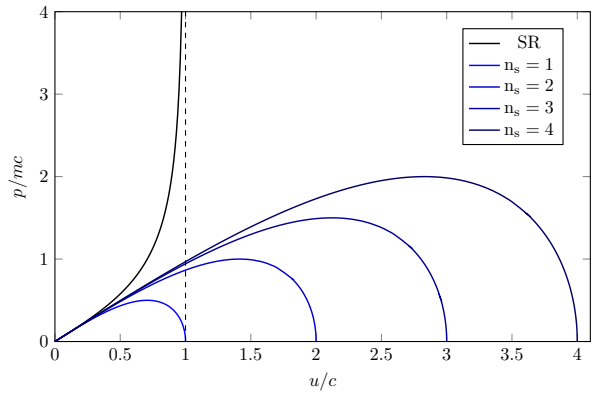

FIG. 8. **Relativistic momentum.** In SR, momentum diverges as velocity increases. With synchronized inertia reduction, momentum rises, peaks, and then decreases to zero as the effective inertia vanishes.

which gives

$$\frac{m_i}{m} = 1 - \frac{U_{\text{align}}}{n_s^2 U_{\text{align,sc}}}. \tag{32}$$

Thus the ratio between coordinate time dt and proper time $d\tau$ becomes

$$\frac{dt}{d\tau} = \left(1 - \frac{U_{\text{align}}}{n_s^2 U_{\text{align,sc}}}\right) \frac{1}{\sqrt{1 - \frac{u^2}{n_s^2 c^2}}}. \tag{33}$$

— *Relativistic energy*. The relativistic energy follows as

$$m_i c^2 = mc^2 \left(1 - \frac{U_{\text{align}}}{n_s^2 U_{\text{align,sc}}}\right) \frac{1}{\sqrt{1 - \frac{u^2}{n_s^2 c^2}}}. \tag{34}$$

When no energy-density gradient is imposed ($U_{\text{align}} = 0$ and $n_s = 1$), this reduces to the familiar special-relativistic expression.

When the propulsion system that couples to the vacuum is activated, the two ratios—the inertia-reduction energy ratio and the velocity ratio—may operate independently (two-layer configuration) or in synchrony (single-layer configuration).

In both cases this yields

$$\frac{U_{\text{align}}}{n_s^2 U_{\text{align,sc}}} = \frac{u^2}{n_s^2 c^2}. \tag{35}$$

Assuming that the time-varying energy-density gradient arises from the moving pattern of a standing wave, whose velocity is determined by a time-dependent phase $\phi(t)$, we apply a phase-dependent velocity similar to that in Ivanov's Rhythmodynamics:

$$u = n_s c \, \frac{\phi(t)}{\pi}, \tag{36}$$

The relativistic energy (FIG. 6) then becomes

$$m_i c^2 = mc^2 \sqrt{1 - \frac{u^2}{n_s^2 c^2}}. \tag{37}$$

For $n_s = 1$, this reproduces the expression obtained by R. L. Carezani [20]:

$$m_i c^2 = mc^2 \sqrt{1 - \frac{u^2}{c^2}}. \tag{38}$$

Although Carezani did not discuss inertia reduction, his reduction of inertial frames to a single effective frame resembles, at a conceptual level, the coupling between the inertial-shielding energy ratio and the velocity ratio in our framework.

— *Relativistic velocity*. In standard relativity,

$$U_k = m_i c^2 - mc^2 = mc^2 \left(\frac{1}{\sqrt{1 - \frac{u^2}{c^2}}} - 1 \right), \tag{39}$$

leading to

$$u = c \sqrt{1 - \left(\frac{1}{1 + \frac{U_k}{mc^2}} \right)^2}. \tag{40}$$

In the modified framework,

$$-U_k = m_i c^2 - mc^2 = mc^2 \left(\sqrt{1 - \frac{u^2}{n_s^2 c^2}} - 1 \right), \tag{41}$$

yielding the velocity–energy relation (FIG. 7)

$$u = n_s c \sqrt{1 - \left(1 - \frac{U_k}{mc^2}\right)^2}. \tag{42}$$

— *Relativistic momentum.* In standard relativity,

$$p = \frac{mu}{\sqrt{1 - \frac{u^2}{c^2}}}. \tag{43}$$

In the modified framework (FIG. 8),

$$p = mu \sqrt{1 - \frac{u^2}{n_s^2 c^2}}. \tag{44}$$

XII. WARP FACTOR

The term "warp factor" originates entirely from the Star Trek franchise, where it served as a narrative device to quantify faster-than-light travel. Over successive series, the warp scale was repeatedly modified to accommodate new storytelling needs.

These changes ranged from simple linear indexing to more elaborate non-linear scales, yet all remained fictional constructs without physical grounding.

Their evolution reflects dramatic requirements rather than scientific principles, and the concept has no correspondence to any parameter used in contemporary theoretical models of spacetime manipulation.

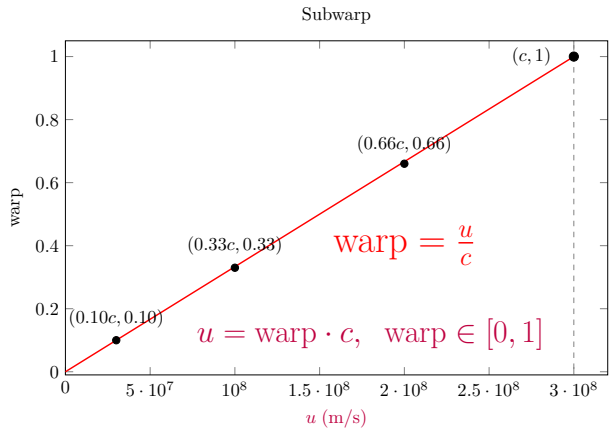

FIG. 9. **Subwarp.** Subluminal regime in which the effective velocity scales linearly with u/c, defining the baseline portion of the proposed warp standard prior to the onset of logarithmic compression.

In contrast to the fictional warp-factor scales introduced by Star Trek, we propose a physically grounded standard derived from the inertial warp-drive concept.

Within this framework, we distinguish two regimes: a linear subluminal domain (FIG. 9) and a logarithmic compression (FIG. 10) of effective velocity beyond c.

The proposed definition is

$$\text{warp} = \begin{cases} u/c, & 0 \le u \le c, \\ \log_3\left(\dfrac{u}{c/3}\right), & u \ge c, \end{cases} \tag{45}$$

which provides an unbounded and reproducible measure of rapid transit while avoiding the arbitrary ceiling effects characteristic of narrative warp scales.

This formulation emphasizes physical realism and operational consistency, reflecting the standards that a technologically mature interstellar civilization would plausibly adopt.

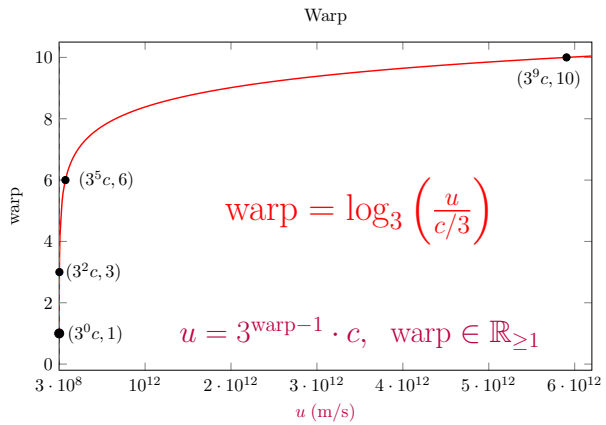

FIG. 10. **Warp.** Superluminal regime in which the logarithmic compression defines an unbounded extension of the warp scale beyond c, providing a reproducible and physically motivated standard for effective velocities exceeding the subluminal domain.

The corresponding velocity associated with a given warp factor is

$$u = \begin{cases} \text{warp} \cdot c, & 0 \le \text{warp} \le 1, \\ 3^{\,\text{warp}-1} \cdot c, & \text{warp} \ge 1. \end{cases} \tag{46}$$

XIII. CONCLUSION

The model developed here treats the vacuum as a continuum of massless spin carriers capable of exchanging momentum with electromagnetic phase structures. Within this framework, a translating phase gradient acts as the fundamental agent of propulsion. The vacuum generates a compensating spin flow, and the reaction to this induced motion produces thrust without propellant. This mechanism accounts for reported electrostatic anomalies and provides a unified physical picture in which thrust, inertia reduction, and phase-controlled energy flow arise from the same underlying interaction. A static phase or energy-density gradient forms an inertial bubble that partially decouples the spacecraft interior from external acceleration. A moving gradient produces a reaction force determined by the direction and magnitude of the phase shift. Because the vacuum permeates all matter, this coupling cannot be shielded, allowing propulsion to operate entirely within closed structures. Momentum conservation is preserved by identifying the vacuum itself as the reaction partner. The present work establishes the theoretical foundation for this mechanism and clarifies the conditions under which it can generate measurable thrust. Extending the analysis to magnetic configurations and maturing the underlying engineering principles may enable a new class of propulsion technologies. Such technologies could scale from laboratory prototypes to planetary and interplanetary vehicles, and eventually to architectures capable of supporting interstellar exploration. Beyond these theoretical implications, the thrust mechanism also enables near-term applications in CubeSat-class probes for Earth-orbit station-keeping and deep-space missions. In these platforms, the primary engineering constraint is not the thrust mechanism itself but the limited specific energy of present-day storage systems. These limits restrict the total electrical energy that can be delivered within a small-mass envelope. Advances in high-density batteries or alternative power sources will therefore be essential to fully exploit the propulsion capabilities implied by the vacuum spin–coupling model and to realize the mission architectures examined in this work.

[1] I. Newton, *Philosophiæ Naturalis Principia Mathematica*, Royal Society, 1687.

[2] A. K. T. Assis, *Weber's law and mass variation*, Physics Letters A, 1989, 136, 277–280.

[3] A. K. T. Assis, *Changing the Inertial Mass of a Charged Particle*, Journal of the Physical Society of Japan, 1993, 62, 1418–1422.

[4] A. K. T. Assis, *Weber's Electrodynamics*, Kluwer Academic, 1994, 10.1007/978-94-017-3670-1.

[5] M. Alcubierre, *The warp drive: hyper-fast travel within general relativity*, Classical and Quantum Gravity, 1994, 10.1088/0264-9381/11/5/001.

[6] J.-L. Naudin, *The PFT Proof of Concept*, JLN Labs, 1999, JLN Labs.

[7] J.-L. Naudin, *The PFT v1.0*, JLN Labs, 1999, JLN Labs.

[8] J.-L. Naudin, *The PFT v2.0*, JLN Labs, 1999, JLN Labs.

[9] J.-L. Naudin, *The PFT v3.0*, JLN Labs, 1999, JLN Labs.

[10] V. F. Mikhailov, *The Action of an Electrostatic Potential on the Electron Mass*, Annales de la Fondation Louis de Broglie, 1999.

[11] S. G. Dimitriou, *Efforts in developing upward and directional thrust*, Presented at the Propellantless Propulsion Conference, University of Sussex, 2001.

[12] V. F. Mikhailov, *Influence of an electrostatic potential on the inertial electron mass*, Annales de la Fondation Louis de Broglie, 2001.

[13] J. P. Wesley, *Inertial Mass Energy Equivalence*, Physics Essays, 2001.

[14] J.-L. Naudin, *The ELG Frolov's Hat experiment*, JLN Labs, 2000, JLN Labs.

[15] J.-L. Naudin, *The Brown-Bahnson Thruster*, JLN Labs, 2002, JLN Labs.

[16] A. Einstein, *On the Electrodynamics of Moving Bodies*, Annalen der Physik, 1905.

[17] A. Einstein, *The Field Equations of Gravitation*, Akademie der Wissenschaften zu Berlin, 1915.

[18] T. T. Brown, *Electrokinetic apparatus*, U.S. Patent 3,187,206, 1965, US3187206.

[19] A. H. Bahnson, Jr., *Electrical thrust producing device*, U.S. Patent 3,227,901, 1966, US3227901.

[20] R. L. Carezani, *Autodynamics: Fundamental Basis for a New Relativistic Mechanics*, SAA Publications, 1998. ISBN 978-0966553307.

[21] Y. N. Ivanov, *Rhythmodynamics*, 2nd Edition, Energia Publishing, 2007. ISBN 978-5-98420-018-9.

[22] R. Kita, *Gravitational attenuating material*, U.S. Patent 8,901,943, 2014, US8901943.

[23] M. Weikert and M. Tajmar, *Investigation of the Influence of a field-free electrostatic Potential on the Electron Mass with Barkhausen-Kurz Oscillation*, Annales de la Fondation Louis de Broglie, 2019, 44, 23–38.

[24] C. R. Buhler and A. N. Aurigema, *System and method for generating forces using asymmetrical electrostatic pressure*, WIPO Patent WO2020159603A2, 2020, WO2020159603A2.

[25] A. V. Frolov, *Propulsion device based on an asymmetric capacitor*, Faraday.ru, 2024, T-Cap.